Separation and Purification Technology 364 (2025) 132400

Contents lists available at ScienceDirect

Separation and Purification Technology

journal homepage: www.elsevier.com/locate/seppur

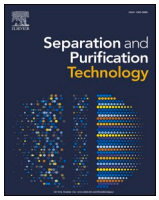

Modelling selective lithium recovery from brines via membrane flow electrode capacitive de-ionization

Giorgio Purpura [a], Hafiz Muhamad Saif [b], Andrea Culcasi [a,*], Sylwin Pawlowski [b,*], Joao Goulão Crespo [b,c], Andrea Cipollina [a]

[a] Dipartimento di Ingegneria, Università Degli Studi di Palermo (UNIPA) – Viale Delle Scienze, Ed 6, 90128 Palermo, Italy
[b] LAQV-REQUIMTE, DQ, FCT, Universidade NOVA de Lisboa, 2829-516 Caparica, Portugal
[c] Instituto de Tecnologia Química e Biológica António Xavier, Universidade NOVA de Lisboa, Av. da República, 2780-157 Oeiras, Portugal

ARTICLE INFO

Editor: Gaohong He

Keywords:
FCDI
Lithium selective membranes
Ion exchange membranes
Process model
Critical raw material

ABSTRACT

The recent growing demand for lithium worldwide, led by the Li-ion battery market, has sparked research into alternative sources of this material. In this context, selective lithium recovery from concentrated brines represents a sustainable and economical alternative to lithium mining activities. In this work, we developed a mathematical model of the recently implemented Lithium Membrane Flow Electrode Capacitive De-Ionization (Li-MFCDI) process, used to selectively extract lithium from a synthetic geothermal brine. The model was validated against the available experimental data and was used to perform a comprehensive parametric analysis. The model predicts the effects of the applied voltage, flow rates, and the adopted membranes on the process performance. These findings highlight the importance of the membrane conductivity-selectivity trade-off for process productivity. Furthermore, this simulation tool will substantially contribute to the development of this novel technology.

1. Introduction

Recently, the growth in the global population and issues with the scarcity of natural resources (e.g., freshwater, essential metals) have increased research interest in alternative, sustainable sources of raw materials. As one of the most in-demand commodities globally, lithium is of significant importance for industry. Indeed, the fast growth of the Li-ion batteries market has markedly increased the demand for lithium, which is expected to rise to 2.43 million tons per year by 2030 [1]. Moreover, lithium is typically produced through environmentally harmful mining activities, and the lithium trade is vulnerable to geopolitical events, as only a few countries, such as Australia, Argentina, and China, have access to the world's most abundant lithium reserves [2]. To reduce the demand for raw lithium and meet the growing global market demand, new non-conventional lithium sources are needed. For instance, geothermal brines and seawater bitterns, which have naturally high lithium concentrations, and thus, these sources are currently under investigation [3–5]. The use of such alternative lithium sources requires an effective way to fractionate complex multi-ionic solutions. However, despite several research efforts, an efficient and environmentally friendly lithium recovery method remains unavailable. Indeed, the selective extraction of lithium from waste brines is hindered by the higher concentrations of other elements, such as sodium, potassium and magnesium, with similar chemical properties [6]. Electro-driven separation technologies, such as ElectroDialysis (ED) and Capacitive De-Ionization (CDI) [7,8], widely adopted for brackish water desalination, have also recently been investigated for the selective recovery of raw materials from concentrated brines [9,10]. In these technologies, the ions are transported by an externally applied electric field, and selective ion transport occurs due to the use of selective Ion-Exchange Membranes (IEMs) or adsorbent electrodic materials [10]. One of the most novel and promising electro-driven separation technologies is Flow Electrode Capacitive De-ionization (FCDI), firstly proposed in 2013 by Jeon et al. [11]. Recently, extensive experimental investigation on FCDI, as a more efficient alternative to conventional CDI, has been carried out to optimize the process [12,13]. The main difference between CDI and FCDI is related to the nature of the electrodes. In both these technologies, ions migrate from the bulk solution towards the electrodic compartments, where they are adsorbed on the porous structure of the electrodes, which act as electrochemical capacitors. However, in conventional CDI, fixed porous electrodes are used to adsorb the ionic species. This feature

* Corresponding authors.
E-mail addresses: andrea.culcasi@unipa.it (A. Culcasi), s.pawlowski@fct.unl.pt (S. Pawlowski).

https://doi.org/10.1016/j.seppur.2025.132400
Received 30 September 2024; Received in revised form 26 February 2025; Accepted 5 March 2025
Available online 6 March 2025

Nomenclature

A_m	Membrane area [m^2]
C	Molar concentration [mol m^{-3}]
$\overline{C}$	Average concentration
C_{el}	Specific capacitance [F kg^{-1}]
d	width [m]
D	Diffusion coefficient [m^2 s^{-1}]
E_{ext}	External electromotive force [V]
F	Faraday constant [C mol^{-1}]
h	height [m]
i_{tot}	Total current [A]
I	Current density [A m^{-2}]
IEC	Ion-Exchange Capacity [mol $kg^{-1}_{dry\ polymer}$]
J	Ionic flux [mol m^{-2} s^{-1}]
L	Length [m]
M	Molar mass [kg mol^{-1}]
N	Number of data points [-]
Q	Flow rate [m^2 s^{-1}]
R	Areal resistance [Ω m^2]
R_g	Universal gas constant [J mol^{-1} K^{-1}]
S	Selectivity [-]
S_{BET}	Specific surface [m^2 g^{-1}]
SEC	Specific energy consumption [kWh kg^{-1}]
SP	Specific productivity [kg m^{-2} $year^{-1}$]
t	Transport number [-]
t_{tot}	Test duration [s]
T	Temperature [K]
v	Linear velocity [m s^{-1}]
V	Volume [m^3]
w_{el}	Mass concentration of suspended particles [kg m^{-3}]
w_u	Water uptake [kg_{water} $kg^{-1}_{dry\ polymer}$]
x	Flow direction
y	Ionic flux direction
z	Ion valence [-]

Greek symbols

δ	Thickness [m]
$\delta_{i,j}$	Kronecker delta [-]
ε	Volumetric fraction [-]
η	Non-ohmic voltage drop [V]
ϑ	Polarization coefficient [-]
κ	Conductivity [S m^{-1}]
φ	Electrostatic potential [V]
ρ_{bulk}	Bulk density [kg m^{-3}]
σ	Charge density [C kg^{-1}]
ω	Mass fraction [-]

Subscript

AEM	Anion exchange membrane
co	Co-ion
cond	Ionic flux conductive component
cou	Counter-ion
diff	Ionic flux diffusive component
D	Donnan
el	Flow electrode/Electrodic compartment
exp.	Experimental point
f	Feed/Feed compartment
fix	Fixed charges
int	Interface
i,j	Component
LiSM	Lithium selective membrane
m	Membrane
N	Nernst
P	Polarization
pred.	Predicted point
r	Receiver/Receiver compartment
s	Solution/Solution compartment
tot	Total
+	Left side
−	Right side

Acronyms

AC	Activated Carbons
AEM	Anion-Exchange Membrane
ARED	Assisted Reverse Electrodialysis
CEM	Cation-Exchange Membrane
CDI	Capacitive De-Ionization
DBL	Diffusion Boundary Layer
ED	Electrodyalisis
EDBM	Electrodyalisis with Bypolar Membranes
EDL	Electrical Double Layer
FCDI	Flow Electrode Capacitive De-Ionization
ICC	Isolated Closed-Cycle
IEM	Ion-Exchange Membrane
LiSM	Lithium Selective Membrane
Li-MFCDI	Lithium Membrane Flow Electrode Capacitive De-Ionization
MRD	Mean Relative Deviation
SC	Single-cycle
SCC	Short-circuited Closed-Cycle
SEC	Specific Energy Consumption
SP	Specific Productivity

makes the process intrinsically non-stationary since, when the electrodes are saturated, they need to be regenerated through short-circuiting or polarity reversal in order to release the adsorbed ions [14]. Conversely, in FCDI, the bulk electrodes are substituted with a slurry, typically made of carbon-based materials such as activated carbons, which are usually pumped through a path carved directly into the current collectors [15]. The carbon particles can then be externally regenerated and recirculated to the electrodic compartment to ensure continuous operation. In 2023, Saif et al. [16] proposed a novel version of FCDI, called Lithium Membrane Flow Electrode Capacitive Deionization (Li-MFCDI), in which a Lithium-Selective membrane (LiSM) was employed to selectively recover lithium from a multi-ionic synthetic geothermal brine. Starting from a multi-ionic solution containing Li^+ and other competing cations such as Na^+, K^+, and Mg^{2+}, the authors were able to separate lithium from the other cations with a process selectivity of 141 ± 5.85 for Li^+/Na^+ and 46 ± 1.46 for Li^+/K^+ and a specific energy consumption of 16.70 ± 1.63 kWh/kg of Li^+ recovered. However, despite these promising results, the effect of the key process parameters, such as the applied voltage and the electrodes' flow rates, on the process performance was not further examined, meaning there is a significant opportunity for process optimization in terms of specific energy consumption and separation efficiency. Nonetheless, further experimental investigation, required to clarify these aspects, would be time-consuming and resource intensive. The use of process models, on the other hand, can help provide insights into the process, guiding toward the best operating conditions while limiting experimental effort. Being a relatively new technology, only a few FCDI process models can be found in the literature [17,18]. Most of these papers focused on the modelling of the electrodic compartments and the electrochemical capacitive phenomena at the electrodes' interfaces and did not account

for the presence of mixed electrolytes. In this work, we aim to propose a simple yet effective model for the Li-MFCDI process, with a focus on the multi-ionic transport phenomena across the IEMs, which are fundamental for this separation process. Such a simple and flexible model can be applied to simulate operation with saline streams of different compositions. The model's equations and structure are first presented, along with its relevant assumptions. Subsequently, the results of the simulations are compared with the experimental data reported by Saif et al. to validate the model. Finally, the Li-MFCDI model is used to perform a parametric analysis, in order to better analyse the influence of the main process variables on the process performance, considering three different LiSMs: the glass ceramic membrane Ohara AG-01; the monovalent-selective polymeric membrane Selemion CSO and an ideal LiSM that merges the best features of both.

2. Description of the simulated system

The following section provides a brief description of the modelled Li-MFCDI unit while fundamental information regarding the experimental procedures can be found in the reference paper [16].

2.1. Li-MFCDI cell

The cell is composed of four separate compartments: the feed and receiver compartments, with identical volumes (10.75 mL) and the two electrodic compartments, which were carved directly into two graphite plates. The feed and receiver compartments are separated by a LiSM, whose effective area inside the cell is 10.75 cm^2, while the electrodic compartments are separated from the solutions compartments using commercial Anion-Exchange Membranes (AEMs). All the cell relevant geometrical properties are reported in Table 1 [16].

The LiSM employed for the experimental campaign is the commercial lithium-conductive glass ceramic membrane AG-01 (Ohara Corporation, Japan), whereas the AEMs (FAB-PK-130, Fumatech BWT, Germany) are dense, reinforced polymeric membranes with high proton-blocking capability, typically employed for ED and EDBM [19]. All the relevant properties of the IEMs adopted for the experimental campaign are reported in Table 2.

Despite the associated error, likely due to the complexity of the measurements, the values of membrane areal resistance and conductivity reported in Table 2 were taken from the manufacturer's technical datasheet, as a direct experimental measurement of these properties falls beyond the scope of the present work. The tests were run in a closed-loop configuration for 7 days, during which an external potential of 1.2 V was applied. The initial composition of the feed, receiver and flow electrodes is reported in Table 3.

2.2. Process configuration

Li-MFCDI can be operated in several process configurations, depending on the recirculating path of the solutions and flow electrodes. Fig. 1 reports a schematic representation of the cell under investigation.

Based on the flow electrodes circulating path, FCDI is typically operated in two main configurations, namely: i) isolated closed-cycle (ICC) and ii) short-circuited closed-cycle (SCC) [13]. In the ICC configuration, the flow electrodes are recirculated separately in the anodic and cathodic tanks and the regeneration is performed by polarity reversal or short-circuiting, thus the process cannot be run in steady-state mode. Conversely, the SCC configuration allows a steady-state operation by regenerating the anodic and cathodic flow electrodes by mixing them in an external reservoir (see Supplementary Material). In this work, a third flow electrode configuration (depicted in Fig. 1) was adopted, namely the Single-Cycle (SC) configuration, in which the flow electrodes are recirculated in closed-loop between the cathodic and anodic compartments. Compared to the configurations above, the latter is easier to implement and allows running the process in a steady-state mode with a lower energy consumption [13,14]. In SC configuration, charge and discharge, which correspond respectively to electro-sorption and desorption of the charged species from the Electric Double Layers (EDLs) of the carbon particles, occur simultaneously in the electrodic compartments, reducing the dissipation of electrostatic energy, thus increasing the energy efficiency of the process [12]. Concerning the flow path of the feed and receivers, the two solutions were externally recirculated in two different tanks in a closed-loop configuration as depicted in Fig. 1. During the process, the feed tank is depleted of Li^+ ions, which migrate towards the receiver's tank. The total volumes and flow rates of the solutions are summarized in Table 4.

Table 1
Geometrical properties of Li-MFCDI unit.

Property	Electrodic channel (el)	Solution channels (s)
Width – d [cm]	0.2	3.7
Heigth – h [cm]	0.2	1.0
Length – L [cm]	27.5	3.7*

* Solution channels are circular; thus, the length corresponds to the width (diameter) of the channels.

Table 2
Relevant properties of FAB-PK-130 and Ohara AG-01 membranes.

	δ [μm]	κ [mS/cm]	R [Ω cm^2]	w_u [g_w/g_{dry}]	IEC [mmol/g_{dry}]	C_{fix} [mmol/g_w]
FAB-PK-130	125 ± 15[20]	1.75 ± 0.75[21]	7 ± 2 [21]	0.1 ± 0.05 [21]	0.85 ± 0.015 [21]	5[20]
OHARA AG-01	250 [16]	0.0019*	12900 *	–	–	–

* The value was fitted from experimental data.

Table 3
The initial composition of feed, receiver and flow electrodes. The flow electrode is a 10 wt% slurry of YP50F activated carbon.

	NaCl [g/L]	KCl [g/L]	LiCl [g/L]	$MgCl_2$ [g/L]	HCl [g/L]
FEED	26.170	0.195	0.096	0.196	0
RECEIVER	0	0	0	0	3.646
FLOW ELECTRODE	1.000	0	0	0	0

3. Modelling

The model developed for the Li-MFCDI process is a 1D pseudo steady-state model with distributed parameters in the flow direction (i.e., ***x***-direction in Fig. 1). Although the simulated closed-loop configuration (as in the experimental set-up) is intrinsically a non-stationary configuration, we assume the time-dependent dynamics of the cell to be negligible compared to the dynamics of the storage tanks. Therefore, in the pseudo steady-state approach, all process variables defined within the Li-MFCDI cell are time-independent. No water transport is assumed across the membranes in the ***y***-direction, as no appreciable volume variation was experimentally observed in the external tanks. Moreover, the diffusive fluxes superimposed on the convective flux in the ***x***-direction are neglected, and the fluid density is assumed to be constant. Finally, no faradic reactions are supposed to take place in the electrodic compartments. In the following sections, the terms "conduction" and "conductive" refer to the fraction of ionic fluxes associated with the passage of current, due solely to the ohmic potential gradient [22]. This term differs from the migrative term commonly reported in the literature, which also accounts for ionic transport due to the diffusion potential that develops in the presence of concentration gradients as a

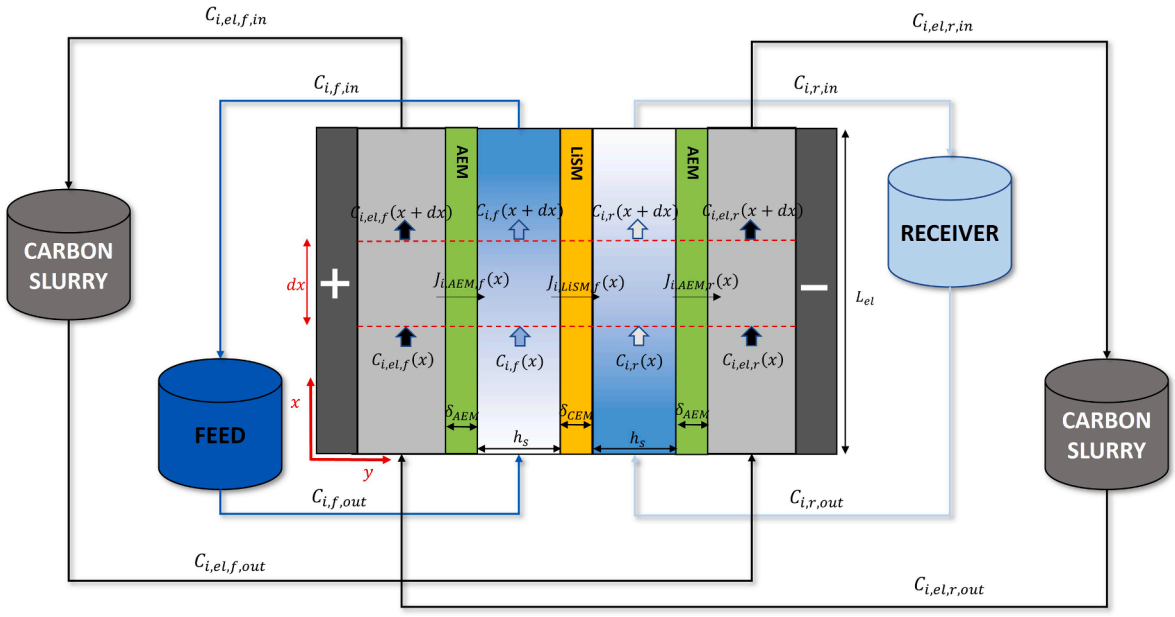

Fig. 1. Schematic representation of the Li-MFCDI cell with Single-Cycle (SC) configuration.

Table 4
Feed, Receiver and flow electrode flow rates and total volume.

	Feed	Receiver	Flow electrodes
V [L]	2	0.2	0.25
Q [mL/min]	10	10	100

result of the differing mobility of ionic species (See section 3.3).

3.1. Mass balance in channels

In order to evaluate the concentration profiles inside the channels, mass balances must be performed for each species. The cell is discretized into 100 elements in the flow direction (i.e., along x), and mass balances are applied to each discretized element in the channels. Taking as positive the fluxes concordant with the y direction and assuming no chemical reaction occurs in the system, the following differential mass balance equations hold:

$$Q_f \frac{dC_{i,f}}{dx} = \left(J_{i,AEM,f} - J_{i,LiSM}\right) d_{el} \tag{1}$$

$$Q_r \frac{dC_{i,r}}{dx} = \left(J_{i,LiSM} - J_{i,AEM,r}\right) d_{el} \tag{2}$$

$$(1-\varepsilon_{el})\, Q_{el} \frac{dC_{i,el,f}}{dx} = -J_{i,AEM,f,diff}\, d_{el} \tag{3}$$

$$(1-\varepsilon_{el})\, Q_{el} \frac{dC_{i,el,r}}{dx} = J_{i,AEM,r,diff}\, d_{el} \tag{4}$$

where $C_{i,f}$ and $C_{i,r}$ are the volumetric molar concentrations (mol m^{-3}) of the species i respectively in the feed and receiver channel at the generic x position; $C_{i,el,f}$ and $C_{i,el,r}$ are the concentrations in the electrodic compartments facing respectively the feed and receiver compartments; Q_f, Q_r and Q_{el} are the volumetric flow rates ($m^3\ s^{-1}$) of the feed, receiver and flow electrodes streams, respectively; d_{el} is the width of the electrodic channels and ε_{el} is the volumetric fraction of suspended solids in the flow electrodes; $J_{i,AEM,f}$ and $J_{i,AEM,r}$ are the total molar fluxes (mol $m^{-2}\ s^{-1}$) of the i-th species across the AEMs facing, respectively, the feed and receiver compartments, while $J_{i,AEM,f,diff}$ and $J_{i,AEM,r,diff}$ correspond to the diffusive component of the total flux across the AEMs. $J_{i,LiSM}$ is the molar flux of the i-th species across the LiSM. In the previous equation, the mass exchange surface (i.e., the active membrane surface) corresponds to the surface of the electrodic channels in contact with the AEMs. Despite the electrodic path tortuosity, the active surface is assumed to be uniformly distributed along the x direction, as this simplifies the expression of the mass balances without appreciably affecting the results of the simulations. The term on the right side of equations (1) and (2) contains all the contributions due to transport phenomena across the IEMs such as ionic diffusion and conduction. Conversely, the right-hand sides of equations (3) and (4) only account for the diffusive component of the flux. Indeed, in the absence of faradic processes, the conductive component of the ionic flux is assumed to be entirely electro-sorbed onto the surface of the carbon particles, thereby it does not cause a net variation in the ionic concentration of the electrodic solution (see section 3.5). The previous equations can be applied to each channel for each ionic species to obtain the concentration profiles in the unit, providing suitable boundary conditions and an expression for the ionic fluxes across the membranes.

3.2. Ionic transport in LiSM

The first LiSM considered in this study is a glass–ceramic membrane with an amorphous glass phase containing dispersed lithium-ion conductive crystal particles which was the one used in the experimental tests. The ion-conduction mechanism in this type of LiSM is the "vacancy diffusion" or "hopping" [23]. Inside the membrane, which can be regarded as a solid-state ionic conductor [23], mobile ions can cross the membrane jumping among the lattice cavities of the crystal structure forced by an applied electric field. The transport rate of each ionic species depends on its jump activation energy, which in turn depends on its ionic radius and the size of the lattice cavities [24]. The selectivity of the membrane towards lithium is due to the size of vacancies in the crystal lattice, which is regulated to be similar to the ionic radius of lithium, thus reducing its activation energy for hopping. Conventional diffusion across this material is assumed to be negligible compared to ionic conduction, due to the very low diffusivities in glassy materials. Consequently, the conductive transport rate of the ionic species across the LiSM can be described by the following equation [22]:

$$J_{i,LiSM} = \frac{t_{i,LiSM}\, I}{z_i F} \tag{5}$$

where z_i and $t_{i,LiSM}$ are, respectively, the valence and the transport number of the i-th species in the LiSM, I is the current density and F is the Faraday constant. In particular, $t_{i,LiSM}$ physically depends on the individual ions' activation energy. However, the measurement of such quantities would require separate physicochemical investigation to be determined, which is beyond the scope of this work. Therefore, ion transport numbers in the LiSM were inferred via calibration of the model on the available experimental data (see paragraph 4.1).

3.3. Ionic transport in AEMs

Ionic transport through dense polymeric membranes, such as the AEMs adopted in the unit, is typically described through the Nernst-Plank equation [20,22]. Assuming a linear concentration profile inside the membrane, the equation can be expressed as follows:

$$J_{i,AEM} = J_{i,AEM,diff} + J_{i,AEM,cond} = -\sum_{j=1}^{n} D_{i,j,AEM} \frac{\left(C_{j,AEM,-} - C_{j,AEM,+}\right)}{\delta_{AEM}} + \frac{t_{i,AEM} I}{z_i F} \tag{6}$$

where $J_{i,AEM}$ is the total ionic flux of the i-th species across the generic AEM, $J_{i,AEM,diff}$ and $J_{i,AEM,cond}$ are the diffusive and conductive component of the total flux, $t_{i,AEM}$ is the average transport number in membrane, δ_{AEM} is the membrane thickness, $C_{j,AEM,-}$ and $C_{j,AEM,+}$ are the molar concentrations of the j-th species in membrane respectively at the right and left interfaces and $D_{i,j,AEM}$ are the cross-diffusion coefficients defined as follows:

$$D_{i,j,AEM} = D_{i,AEM}\delta_{i,j} + t_{i,AEM}\frac{z_j}{z_i}\left(D_{i,AEM} - D_{j,AEM}\right) \tag{7}$$

where $D_{i,AEM}$ and $D_{j,AEM}$ are respectively the ionic diffusion coefficients of the i-th and j-th species in the membrane phase, while $\delta_{i,j}$ is the Kronecker delta, which assumes the value of 1 or 0 when $i = j$ and $i \neq j$, respectively. Equation (6) presents the diffusion-conduction form of the Nernst-Plank equation, derived from the traditional diffusion-migration form by substituting the total electric potential gradient with the sum of the ohmic and diffusion potential gradients [22]. Indeed, the cross-diffusion coefficients are defined to take into account the diffusion potential arising as a consequence of the electrical coupling of charged species fluxes in a neutral system [22]. The transport numbers in the membrane, $t_{i,AEM}$, can be related to the diffusivity and average concentration in the membrane of each ionic species, according to the following equation:

$$t_{i,AEM} = \frac{z_i^2 \, D_{i,AEM} \, \overline{C}_{i,AEM}}{\sum_n z_j^2 \, D_{j,AEM} \, \overline{C}_{j,AEM}} \tag{8}$$

where $\overline{C}_{i,AEM}$ is the average concentration in the membrane of the i-th species. Note that equation (8) can be applied to evaluate the transport number in solution by substituting the diffusivities and average concentrations in the membrane with the ionic diffusivities and concentrations in the bulk solution. In order to apply equation (6), the equilibrium concentrations of each mobile species at each solution-membrane interface must be known. When an ion-exchange membrane is contacted with an electrolytic solution, mobile ions are absorbed inside the membrane to satisfy the electrochemical equilibrium at the solution-membrane interface. Because of the presence of fixed charged groups inside the polymeric matrix, the ions bearing a charge opposite to the fixed charges (i.e., the counter-ions) are preferentially sorbed within the membrane. On the contrary, the sorption of ions with charges similar to the fixed charges (i.e., co-ions) is hindered, according to the well-known mechanism of Donnan exclusion [7]. A qualitative representation of the concentration and potential profile across a generic AEM is reported in Fig. 2.

Assuming an ideal behavior of each thermodynamic phase, ion

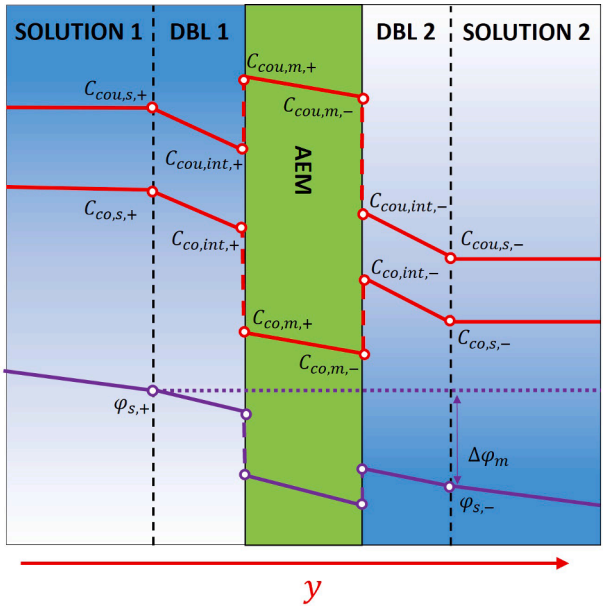

Fig. 2. Qualitative representation of concentration and potential profile across a generic AEM. The superscript + and – denote, respectively, the left and right side of the membrane, according to the chosen y direction. The subscripts "cou" and "co" refer to a generic counter-ion and co-ion in a multi-ionic solution. The superscript s, m and int refer to, the bulk solution, membrane phase and solution-membrane interface, respectively.

partitioning between the AEMs and the external solutions can be described using the ideal Donnan equilibria [7,25]:

$$C_{i,AEM} = C_{i,int} exp\left(-\frac{z_i F}{R_g T}\Delta\varphi_D\right) \tag{9}$$

where $C_{i,AEM}$ is the equilibrium concentration of the i-th species at the membrane side of the interface, $C_{i,int}$ is the concentration at the solution side of the interface, R_g is the ideal gas constant, T is the absolute temperature and $\Delta\varphi_D$ is the Donnan potential, i.e., the potential difference arising at the solution-membrane interface due to the difference in the counter-ions concentration between the two phases [26]. The equilibrium concentrations of the ions in the membrane phase are also related to each other by the electroneutrality condition, which states that the net charge density in the membrane phase must be null everywhere:

$$\sum_i z_i C_{i,AEM} + z_{fix} C_{fix} = 0 \tag{10}$$

where z_{fix} is the valence of the fixed charges (usually equal to 1) and C_{fix} is the concentration of fixed charges in the membrane phase. Given the solution-side interface concentrations, equations (9) and (10) form a finite set of equations that can be applied to each side of the AEMs to obtain the equilibrium concentrations of the ions in the membrane phase.

3.4. Concentration polarization phenomena

Concentration polarization typically arises at the interface between the solution and membrane phases because of the diverse ions' transport numbers in the two phases [7,8]. This phenomenon is typically quantified in terms of polarization coefficients, defined as the ratio between the interface concentration and the bulk concentration [20,27]:

$$\vartheta_i = \frac{C_{i,int}}{C_{i,s}} \tag{11}$$

where ϑ_i is the polarization coefficient at a generic solution-membrane

interface and $C_{i,s}$ is the concentration of the i-th species in the bulk solution. In the classical approach, the polarization coefficients can be evaluated by performing a steady-state mass balance at the DBL, applying Fick's law to describe the diffusion of the neutral salt using an average diffusion coefficient [28]. However, such an approach is rather cumbersome in a multi-ionic system. A rigorous formulation can be obtained by expressing the ionic fluxes through the Nernst-Plank equation (6) into the mass balance at the DBL. Neglecting the contribution of the diffusive flux across the membrane, which is negligible (due to the low concentrations and high permselectivity of the membranes) and often neglected in similar studies [7], the following formulation for the polarization coefficients can be obtained:

$$\vartheta_{i,+} = 1 - \frac{\frac{(t_{i,m}-t_{i,s,+})I}{z_i F} - \sum_{j\neq i}\frac{D_{i,j,s}}{\delta_{j,DBL,+}}C_{j,s,+}\left(1-\vartheta_{j,+}\right)}{\frac{D_{i,s}}{\delta_{i,DBL,+}}C_{i,s,+}} \tag{12}$$

$$\vartheta_{i,-} = 1 + \frac{\frac{(t_{i,m}-t_{i,s,-})I}{z_i F} - \sum_{j\neq i}\frac{D_{i,j,s}}{\delta_{j,DBL,-}}C_{j,s,-}\left(1-\vartheta_{j,-}\right)}{\frac{D_{i,s}}{\delta_{i,DBL,-}}C_{i,s,-}} \tag{13}$$

in the previous equation, $+$ and $-$ identify the left and right side of the membrane (consistently with the direction of the current density), $t_{i,s}$ and $t_{i,m}$ are respectively the transport numbers in the bulk solution and in the generic membrane while $\delta_{i,DBL}$ is the DBL thickness. The difference between the original formulation and the previous one lies in an extra contribution at the numerator, accounting for the electrical coupling of the ionic fluxes (theoretical derivation of equations (12) and (13) can be found in Supporting Material). Equations (12) and (13) can be written for each species to get a system of linear equations that can be solved to evaluate the polarization coefficients at both membrane interfaces. In the absence of mixing promoters and for not fully developed flow, the DBL thickness can be estimated through the Leveque equation [29,30]:

$$\delta_{i,DBL} = \frac{h_s}{1.47}\left(\frac{d_s D_{i,s}}{h_s^2 v_s}\right)^{1/3} \tag{14}$$

where h_s and d_s are respectively the height and diameter of the channel and v_s is the fluid velocity (m s^{-1}) that can be evaluated from the flow rate. Equation (14) can be reasonably applied to the feed and receiver channels but not to the electrodic compartments. In fact, given the particular geometry and flow field of the electrodic channels and considering that flow electrodes are structured fluids, a specific CFD analysis should be performed to obtain Sherwood number correlations to estimate $\delta_{i,DBL}$. However, according to the correlation proposed by Rommerskirchen et al. [17], the DBL thickness in the electrode compartments is less than 3 % of that in the feed and receiver channels. This implies that, under the applied process conditions, concentration polarization in the electrode compartments is negligible in comparison with the other compartments. Therefore, in the present study, only polarization phenomena in the solutions' channels are considered.

3.5. Circuital equations

In order to evaluate the ionic fluxes (equations (5) and (6)) and solve the mass balances in each compartment, the current density associated with the conductive term of the fluxes must be calculated. Given the distributed nature of the model, the current density profile along the ***x***-direction can be obtained by solving an equivalent distributed electrical circuit in which each circuital component (i.e., resistances, capacitances and electromotive forces) corresponds to an element of the unit (i.e., membranes, electrodes and solutions). A qualitative potential profile inside the cell is depicted in Fig. 3, along with the chosen equivalent circuital elements.

Assuming the current collectors are equipotential surfaces, the resulting equivalent circuital model is a distributed parallel circuit made of a certain number of branches, all subjected to the same applied voltage, as depicted in Fig. 4. Consequently, if not differently specified, all the electrical variables that will be henceforth introduced will be distributed along the ***x***-direction.

Regarding the flow electrodes, various circuital models have been proposed to describe the electrical response due to the presence of porous carbon particles [31]. According to the so-called "vertical ladder model", in the presence of particles with a non-uniform pore size distribution and at very low current frequencies, the flow-electrodes can be conveniently described as a parallel of resistances and capacitances in series (as depicted in Fig. 4), which usually corresponds to the capacitance reported by the manufacturer for the specific material [32,33]. Therefore, the potential drop throughout each flow electrode can be

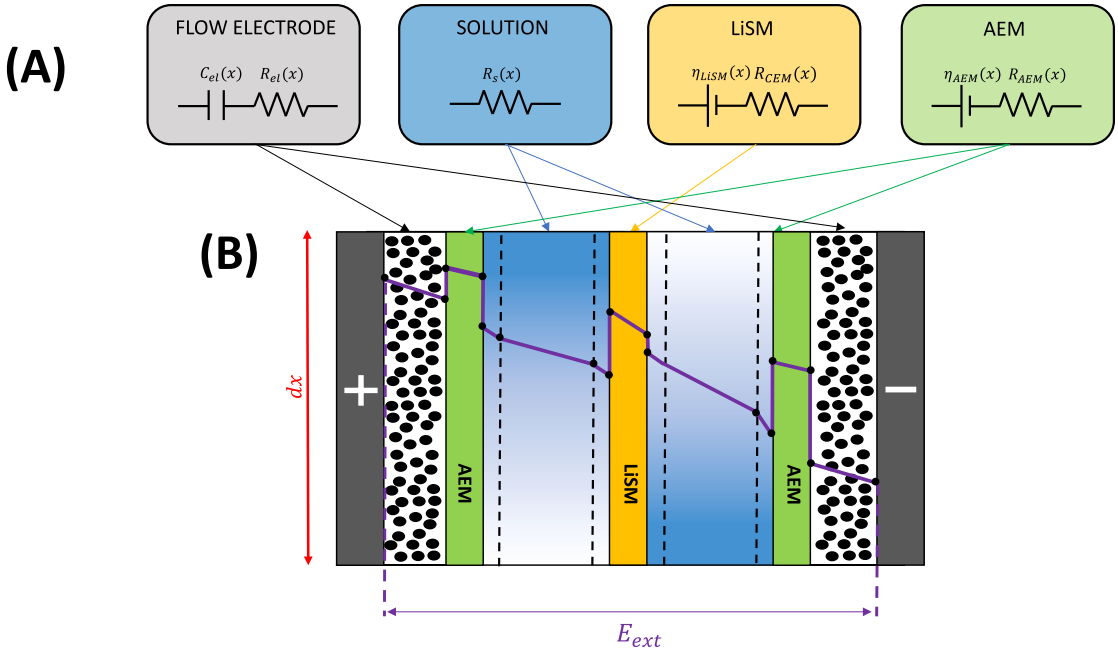

Fig. 3. (A) Equivalent electrical components for flow electrodes, ion-exchange membranes and solutions. (B) Qualitative potential profile across the electrodes.

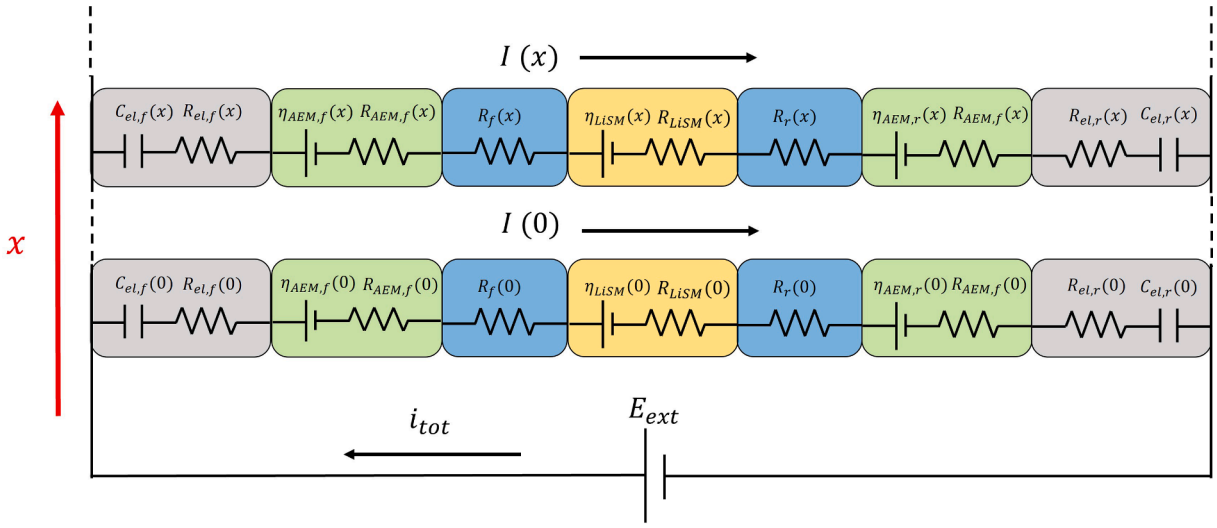

Fig. 4. Equivalent electrical circuit of the Li-MFCDI cell, with the x-direction discretisation of all variables.

evaluated withthe following equation:

$$\Delta\varphi_{el} = \frac{\sigma_{el}}{C_{el}} + R_{el} I \tag{15}$$

where C_{el} is the specific capacitance of the carbon particles per unit of mass, σ_{el} is the charge density accumulated on the carbon particles at the generic x position, and R_{el} is the equivalent areal resistance. In general, the resistive behaviour of the flow electrodes is related to different contributions. It depends on various parameters such as the carbon loading, the salt concentration, the flow rates and, of course, the nature of the carbon material. The equivalent conductivity adopted in the present work was measured by Porada et al. for a carbon slurry of similar composition to the one used in this study (10 % YP50F in 1 g/L NaCl) [34]. This conductivity is mainly related to the electronic conductivity of the carbon particles, which would represent the main contribution to the total areal resistance of the flow electrode. Following their approach, the equivalent resistance of the flow electrodes was evaluated through the following equation:

$$R_{el} = \frac{h_{el}}{\kappa_{el}} \tag{16}$$

where h_{el} is the electrodic channel depth, and κ_{el} is the carbon slurry equivalent conductivity, assumed to be constant. All the required carbon slurry properties were taken from the literature and are reported in Table 7. Concerning the electrical behaviour of the membranes, they can be modelled as a series of resistance and electromotive force. Therefore, the overall potential drop across the membrane, $\Delta\varphi_m$, can be expressed as follows:

$$\Delta\varphi_m = R_m I + \eta_P + \eta_N \tag{17}$$

where R_m is the membrane areal resistance while η_P and η_N represent the non-ohmic voltage drop, respectively due to the concentration polarization at the two solution-membrane interfaces, and the Nernst potential raise/drop across the membrane due to the concentration difference of the two solutions facing the membrane itself. Note that the subscript m refers to a generic membrane, including the LiSM. Assuming ideal thermodynamic behaviour and linear concentration profiles across the membrane, and considering the average transport numbers for the ionic species, the well-known Nernst equation [25] can be used to evaluate the non-ohmic potential drop across the membrane:

$$\eta_m = \eta_P + \eta_N = \frac{RT}{F}\sum_i \frac{t_{i,m}}{z_i} ln\left(\frac{\theta_i^-}{\theta_i^+}\right) + \frac{RT}{F}\sum_i \frac{t_{i,m}}{z_i} ln\left(\frac{C_{i,s,-}}{C_{i,s,+}}\right) \tag{18}$$

Although η_m is defined as a voltage drop, its sign depends on the difference in concentration between the two compartments facing the membrane. Consequently, η_m could provide a net negative contribution, acting as an electromotive force. The feed and receiver channels behave like simple ohmic resistances and, thus, can be straightforwardly modelled through Ohm's law as follows:

$$\Delta\varphi_s = \frac{h_s}{\kappa_s} I \tag{19}$$

where κ_s is the conductivity of the generic solution and h_s is the height of the solution channels (reported in Table 1). κ_s depends on the ionic concentration of the solution and was evaluated by applying the McCleskey model [35]. Ultimately, the current density in each branch of the equivalent circuit can be evaluated by applying the second Kirchhoff's law, according to which the sum of the voltage drops along the branch must be equal to the applied electric potential:

$$E_{ext} = \sum_i \Delta\varphi_i = \Delta\varphi_{el,f} + \Delta\varphi_{AEM,f} + \Delta\varphi_f + \Delta\varphi_{LiSM} + \Delta\varphi_d + \Delta\varphi_{AEM,r} + \Delta\varphi_{el,r} \tag{20}$$

By substitution of the previous equations ((15)–(19)) and following rearrangements of terms, equation (20) can be rewritten as follows:

$$E_{ext} = \frac{\sigma_{el,f} + \sigma_{el,r}}{C_{el}} + R_{tot} I + \eta_{m,tot} \tag{21}$$

where R_{tot} is the sum of areal resistances of flow electrodes, membranes and solutions, $\eta_{m,tot}$ is the sum of the membranes non-ohmic voltage drops, while $\sigma_{el,f}$ and $\sigma_{el,r}$ are the charge densities accumulated on the carbon particles at a certain position x, which are related to the current density by the following charge balance equation:

$$I = -\frac{Q_{el} w_{el}}{d_{el}} \frac{d\sigma_{el,f}}{dx} = \frac{Q_{el} w_{el}}{d_{el}} \frac{d\sigma_{el,r}}{dx} \tag{22}$$

where w_{el} is the mass concentration of suspended AC. Equations (21) and (22) form a system of ODEs that can be solved numerically, along with mass balances and transport equations, to obtain the charge and current density profiles along the flow direction. Finally, the total current can be straightforwardly evaluated by integration of the current density:

$$i_{tot} = \int_0^{L_{el}} I d_{el} dx \tag{23}$$

3.6. Mass balance in tanks

The set of equations presented in the previous paragraphs can be solved to obtain the steady-state concentration and current density profiles inside the cell. However, the lithium recovery process is intrinsically non-stationary, as in the closed-loop configuration, the concentration of each species in the storage tanks changes over time. The following mass and charge balances are then applied to the tanks to evaluate the change in concentration of each species and charge density onto the carbon particles over time:

$$V_f \frac{dC_{i,f,out}}{dt} = Q_f\left(C_{i,f,in} - C_{i,f,out}\right) \tag{24}$$

$$V_r \frac{dC_{i,r,out}}{dt} = Q_r\left(C_{i,r,in} - C_{i,r,out}\right) \tag{25}$$

$$\frac{V_{el}}{2} \frac{dC_{i,el,f,out}}{dt} = Q_{el}\left(C_{i,el,f,in} - C_{i,el,f,out}\right) \tag{26}$$

$$\frac{V_{el}}{2} \frac{dC_{i,el,r,out}}{dt} = Q_{el}\left(C_{i,el,r,in} - C_{i,el,r,out}\right) \tag{27}$$

$$\frac{V_{el}}{2} \frac{d\sigma_{el,f,out}}{dt} = Q_{el}\left(\sigma_{el,f,in} - \sigma_{el,f,out}\right) \tag{28}$$

$$\frac{V_{el}}{2} \frac{d\sigma_{el,r,out}}{dt} = Q_{el}\left(\sigma_{el,r,in} - \sigma_{el,r,out}\right) \tag{29}$$

In the previous equations, V_f, V_r and V_{el} are, the total volume of feed, receiver and carbon slurry, respectively, Q_f, Q_r and Q_{el} are their volumetric flow rates, while $C_{i,f,out}$, $C_{i,r,out}$, $C_{i,el,f,out}$ and $C_{i,el,r,out}$ are the ionic concentrations of the i-th species in the solutions and electrodic tanks, corresponding to the inlet concentration in the unit (i.e. concentration evaluated at $x = 0$), $C_{i,f,in}$, $C_{i,r,in}$, $C_{i,el,f,in}$ and $C_{i,el,r,in}$ are the tanks' inlet concentrations, corresponding to the outlet concentrations from the unit (i.e., evaluated at $x = L$) , $\sigma_{el,f,out}$ and $\sigma_{el,r,out}$ are the charge densities accumulated onto the carbon particles in the two electrodic tanks, corresponding to the inlet charge densities in the two electrodic compartments, while $\sigma_{el,f,in}$ and $\sigma_{el,r,in}$ are the tanks' inlet charge densities, corresponding to the charge densities accumulated at the outlet of the unit's electrodic compartments.

4. Results and discussion

The following section compares the outcomes of the simulations performed with the proposed model with the experimental data collected by Saif et al. [16]. The developed model is then used to perform a parametric analysis to understand the impact on the lithium recovery process of the main parameters, such as applied voltage, flow rates, and flow electrodes' properties, providing deep insight into the main dependences affecting the Li-MFCDI unit performance. The Li-MFCDI model was utilized to simulate the performance of the unit using different types of LiSM. Particularly, the Ohara AG-01 LiSM was compared with the Selemion CSO cation-exchange membrane (Asahi Glass Company, Japan) and an ideal LiSM that integrates the best features of both. All the simulations were carried out using MatLab® and concern tests with a total process time of 7 days.

4.1. Model parameters

In order to apply the model presented in the previous sections, transport numbers in the LiSM and ionic diffusivities in the AEMs, which are specific properties of the membrane/ions, were determined through a fitting procedure based on the experimental time-concentration trends observed in the receiver tank. Instead, the areal resistance of the Ohara AG-01 membrane was directly obtained from the experimental current-voltage profile. The input membrane parameters are reported in Table 2 and the resulting fitting parameters are listed in Table 5.

For comparison purposes, the model was used to predict process performance when different types of LiSMs were employed. The properties of the LiSMs used for comparison are listed in Table 6.

Transport parameters for the comparison LiSMs were similarly retrieved from the experimental data reported by Nie et al. [36] and are provided in Table 5. Further discussion about the fitting procedure can be found in the Supporting Material.

4.2. Model validation

The model was tested against the experimental data collected in a previous work presenting the operational data of a Li-MFCDI unit using the Ohara AG-01 membrane [3]. This test was executed under the process conditions reported in Table 3 and Table 4. The applied voltage was set to 1.2 V. The main results are reported in Fig. 5. Since the volume of the feed solution was ten times that of the receiver solution, no appreciable variation in concentration occurred in the feed tank after 7 days; thus, only the receiver tank concentration was reported. As shown in Fig. 5A, we successfully calibrated the model using experimental concentration data, thereby validating its applicability. The experimental concentration profiles in the receiver tank are substantially linear because the main transport mechanism of the cations from the feed to the receiver compartment is of conductive type. Therefore, the slope of the concentration vs. time profiles can be related to the transport numbers of the ionic species: the steeper the slope, the greater the passage of the ionic species through the LiSM. Indeed, conventional diffusion across a dense ceramic material, such as the one of the adopted LiSM, is supposed to be strongly hindered. In this way, the proposed model quantitatively predicts the concentration profiles in the receiver tank.

Another variable monitored during the test was the receiver compartment pH, which is reported in Fig. 5B. As the adopted receiver is a 0.1 M HCl solution, H^+ can move from the receiver compartment across the adjacent membranes either by diffusion or conduction. The proposed model captures the increase in pH in the receiver compartment. However, as shown in Fig. 5B, from a quantitative stand point, the pH variation in the receiver tank after 7 days is negligible and corresponding to a H^+ concentration difference of less than 0.01 M. As discussed before, conventional diffusion across the LiSM is hindered. Consequently, pH variation in the receiver tank has to be attributed to H^+ transport across the adjacent AEM. Nevertheless, the anionic membrane used in the tests (FAB-PK-130) are known to have very good proton-blocking properties [21]. Hence, H^+ transport from the receiver compartment is strongly impeded in both directions. Therefore, according to the model, under the proposed operating conditions, the use of HCl as a supporting electrolyte in the receiver compartment is not expected to reduce the specific energy consumption. The current obtained from the simulation under potentiostatic conditions was substantially constant around 0.05 mA, similar to what was observed during the experimental test. This result suggests that the electrical behavior of the system is stable as well, and therefore it can be conveniently described through a pseudo-steady-state model. To clarify the significance of each element in the equivalent electric circuit of the unit on the applied external potential, the individual contributions to the total potential drop are illustrated in Fig. 6A. The main contribution is provided

Table 5
FAB-PK-130, Ohara AG-01, Selemion CSO and Ideal LiSM parameters obtained from experimental data fitting.

	Na^+	K^+	Li^+	H^+	Mg^{2+}	Cl^-
$D_{i,AEM}$ [m^2/s]	0	0	0	6.7E-10	0	1.12E-10
$t_{i,AG-01}$	0.400	0.009	0.310	0	0.041	0.240
$t_{i,CSO}$	0.989	0.006	0.004	0	0.001	0
$t_{i,IDEAL\ LiSM}$	0.319	0.322	0.273	0	0.086	0

Table 6
Properties of the Selemion CSO and of the ideal LiSM. For the sake of comparison, the main properties of the Ohara membrane (already reported in Table 2) are reported below as well.

	δ_{iem} [μm]	κ_{iem} [mS/cm]	R_{iem} [Ω cm^2]	w_u [g_w/g_{dry}]	IEC [mmol/g_{dry}]	C_{fix} [mmol/g_w]
SELEMION CSO	100	4.35	2.3	0.2–0.25	2	8.9
IDEAL LiSM	100	4.35	2.3	0.2–0.25	2	8.9
OHARA AG-01	250	0.1	250	–	–	–

by the ohmic drops, while a negligible contribution is provided by the polarization phenomena at the interfaces of the membranes. This is clearly due to the very low current density achieved during the operation (around 0.1 A/m^2). In fact, according to equations (12) and (13), the magnitude of polarization phenomena increases at high current density while it is negligible at low current density [8,29]. The overall contribution of Nernst potential is negative, i.e., it provides an additional electromotive force to be added to the external potential. This non-negligible contribution must be ascribed to the adopted process configuration in which the LiSM is used to separate a highly concentrated feed solution from a dilute receiver. Consequently, the units work similarly to an Assisted-Reverse Electrodialysis (ARED) cell, where the spontaneous salt transport from the more concentrated compartment to the less concentrated compartment is further promoted thanks to an externally applied electric field [37].

The capacitive contribution to the overall voltage drop is not reported because, according to the assumption reported in the modelling section, the capacitive flow electrodes are modelled as ideal capacitors in charging and discharging phases. Hence, in a steady-state condition and assuming a symmetric charge distribution on the two electrodes, the net capacitive voltage drop is zero. Although not strictly true, this result aligns with the previous literature, indicating that in a closed-loop configuration, the capacitive contribution of the electrodes minimally impacts the performance of the unit [38]. The results of the analysis suggest that, in order to reduce the system's energy loss, greater effort should be focused on minimizing the unit's ohmic losses. To further investigate the origin of these losses, an analysis of the ohmic voltage drops is presented in Fig. 6B, showing the percentage contribution of each source to the overall ohmic drop. The results clearly demonstrate that the primary contributor to the unit's overall electrical resistance is the LiSM, accounting for over 90 % of the total areal resistance. This fact is attributed to the Ohara AG-01 structure characterized by an extremely low ionic conductivity. Unlike conventional polymeric membranes, this non-porous ceramic material does not absorb water. Consequently, ion mobility within the membrane phase is significantly limited, leading to poor ionic conductivity. The second major factor contributing to ohmic voltage drops is the electrical resistivity of the electrodic compartments. All other resistances are essentially negligible. In conventional FCDI processes, the dilute compartment contributes non-negligibly to the ohmic drops due to the low conductivity of the desalinated solution. However, in this work, a diluted HCl solution was used as the receiver stream, thus markedly reducing the solution resistivity, thanks to the high mobility of H^+ ions.

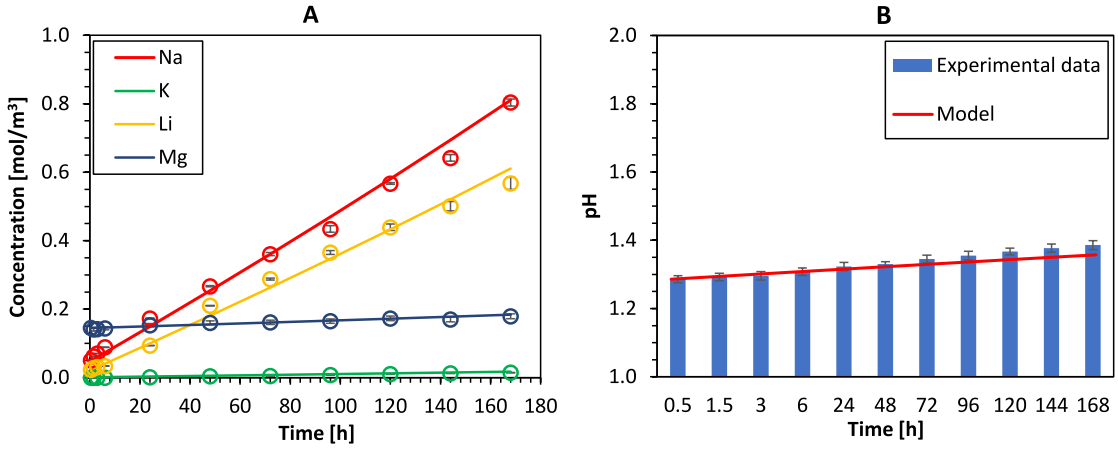

Fig. 5. (A) Concentration of species in the receiver tank vs time. The empty circle represents the experimental data while the solid lines represent the model prediction. (B) Receiver compartment pH versus time. The blue columns represent the experimental data while the solid red line represents the model prediction. Membrane: Ohara AG-01. (For interpretation of the references to colour in this figure legend, the reader is referred to the web version of this article.)

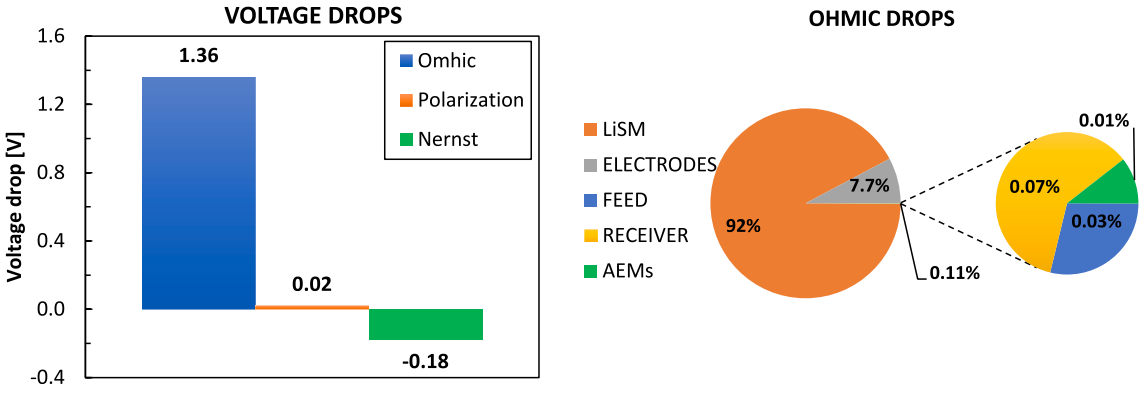

Fig. 6. (A) Average voltage drops in the Li-MFCDI unit. (B) Ohmic drops percentage contributions. Membrane: Ohara AG-01.

4.3. Effect of voltage and flow rates

In order to understand the effect of the applied voltage and solutions' flow rate on the lithium recovery process, a parametric analysis was performed. Although the model was developed under the assumption that no faradaic reactions occur at the electrodes—an assumption which remains valid provided that the externally applied potential is not excessively high—a parametric analysis was nonetheless performed by varying the applied voltage to investigate its effect on lithium recovery. The Specific Energy Consumption (SEC) and the lithium Specific Productivity (SP), respectively expressed in terms of kWh kg^{-1} of recovered lithium and kg m^{-2} $year^{-1}$, are used to quantify the Li-MFCDI unit performances:

$$SEC = \frac{\int_0^{t_{tot}} E_{ext}\ i_{tot}\ dt}{3.6\ 10^6\ \Delta C_{Li,r,out} V_r\ M_{Li}} \tag{30}$$

$$SP = \frac{3.154\ 10^7\ \Delta C_{Li,r,out}\ V_r\ M_{Li}}{A_m\ t_{tot}} \tag{31}$$

In equations (30) and (31) $\Delta C_{Li,r,out}$ is the variation of the lithium molar concentration in the receiver tank, M_{Li} is the lithium molar mass, A_m is the membrane area while t_{tot} is the overall test duration. All the simulations were performed over a simulated time of 7 days at the same initial concentrations adopted for the model validation. The results are reported in Fig. 7 A and B. The estimated value of SEC at 1.2 V and 10 mL/min is 12.7 kWh/kg_{Li} (i.e., per kilogram of recovered lithium), with a SP of 7.9 $kg_{Li}/(m^2\ year)$, corresponding to a productivity of 0.131 $mol_{Li}/(m^2\ h)$. According to the simulation performed, the previous value could be reduced to 2.3 kWh/kg_{Li} by reducing the applied voltage to 0.5 V. Conversely, an increase in the applied voltage results in an increase in both SEC and SP by 10.6 kWh/kg_{Li} and 5.8 $kg_{Li}/(m^2\ year)$, corresponding to a productivity of 0.096 $mol_{Li}/(m^2\ h)$) per unit of applied voltage respectively. These productivity values are relatively low compared to other similar technologies [39] due to the high lithium selectivity of the adopted LiSM. Indeed, high selectivity is associated with lower ionic conductivity, i.e., lower ionic recovery. Conversely, high ionic conductivity allows achieving high SP but results in lower separation selectivity. The results of the simulation indicate that doubling the SP by increasing the applied voltage leads to a fourfold increase in SEC. The rise in SEC and SP is due to the increase in current density, which grows linearly with the applied voltage. In fact, this causes an increase of the ohmic losses, which are proportional to the current, but also of the SP which is related to the lithium recovery and hence to the partial current density carried by lithium ions. The linear trend in SEC and SP is likely to be an artifact due to the assumption of AEMs ideal selectivity. Rigorously, the increase in SP should reduce at high applied voltage because of the diffusion of lithium from the receiver toward the electrodic compartment. However, the maximum lithium recovery obtained corresponds to less than 16 % (at 8 V applied voltage). Even in this condition, the concentration gradient between the receiver and the cathodic compartment would likely result in a negligible lithium diffusive flux, given the very low concentration achieved in the receiver compartment and the very low partitioning coefficient of lithium in conventional polymeric IEMs [40,41]. Consequently, the AEMs ideal behaviour assumption (i.e., no diffusive flux of cations except for H^+) will not cause a consistent deviation between the simulations and the experimental outcome. It is worth noting that, although the model does not take into account Faradaic reactions, the model is still valid as the potential electro-chemical reactions at the electrodes are not directly related to the ionic transport across the LiSM.

The effect of the feed and receiver flow rates on the recovery performance was investigated as well. The simulations were performed changing simultaneously the flow rates in both the feed and receiver compartments. The SEC evaluated at different flow rates and applied voltages is reported in Fig. 7B. According to the simulations, the SEC is only slightly influenced by the flowrates of the feed and receiver solutions, with a very slight decrease for high flowrates at high applied voltage. In particular, the SEC decreases by only 0.8 % when increasing the flowrates from 5 to 100 mL/min. However, this slight reduction would likely be offset by the increased pumping power. Therefore, the results suggest that, under the chosen operating conditions, the solution flow rate is not an effective optimization decision variable. This can be explained by considering that the effect of flowrates on the SEC arises from the polarization phenomena, which tend to reduce the available electromotive force. Typically, polarization phenomena decrease when the mixing condition in the channels improves. However, as previously discussed, polarization phenomena have a minor impact on the overall energy efficiency of the process due to the low current density achieved and, thus, changing the flow rates have no appreciable impact on the SEC. Nevertheless, the mathematical modeling of polarization phenomena is important, as they may not be negligible in the case of polymer membranes. Moreover, taking also into account the power consumption of the pumps, an increase in the flow rates would increase the energy consumption of the process, making working at high flowrates inconvenient.

4.4. Effect of flow electrodes' composition

In conventional FCDI, the flow electrodes play a significant role in

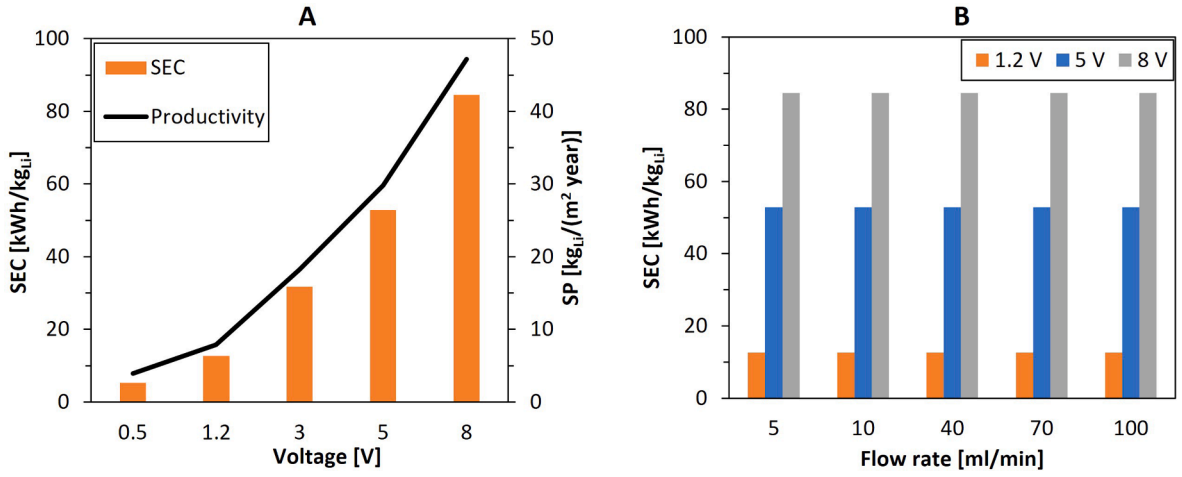

Fig. 7. (A) Specific Energy Consumption (SEC) and lithium Specific Productivity (SP) versus applied voltage at flow rates of 10 mL/min (See Table 4). (B) SEC versus feed and receiver flow rates at different applied voltages.

the overall process performance. Changing the composition of the flow electrodes may have a considerable impact on the operation. For instance, using different types of activated carbon may lead to variations in conductivity and capacitance, influenced by factors such as pore size distribution, specific surface area, and the intrinsic electronic conductivity of the material [42–44]. To explore the impact of varying flow electrode compositions, simulations were performed using different types of activated carbons selected among the most commonly available commercial types. The properties of the flow electrodes used in the simulations are detailed in Table 7.

The results of the simulations are reported as SP vs SEC curves in Fig. 8. For all the ACs investigated, the SP is linearly related to the SEC. Consequently, the maximum achievable SP corresponds to the maximum achievable SEC, which is typically evaluated through a techno-economic assessment. The linear trend is associated with the absence of detrimental phenomena under the applied operating conditions, apart from ohmic losses and diffusive fluxes. At fixed SEC, the SP achieved using YEC200D and Norit SX Ultra AC is almost equal and only slightly higher than the one achieved with the YP-50F adopted by Saif et al.. This result can be attributed to the higher electronic conductivity of these ACs, as reported in Table 7. The difference in SP between the reference and comparison AC becomes more pronounced at higher SEC, as ohmic losses increase with higher current densities. However, the most significant difference in SP observed at 8 V amounts to only 6 %. This result is related to the high resistance of the LiSM investigated, compared to the flow electrode resistance. The effect of the LiSM properties, such as ionic conductivity, will be further examined in paragraph 4.5.

4.5. Effect of LiSM properties

Based on the analysis presented earlier, the performance of the Li-MFCDI unit is only marginally affected by operating conditions and the composition of the flow electrodes. However, it is significantly influenced by the properties of the selected LiSM, particularly the ionic conductivity of the membrane. Therefore, simulations were performed to compare the performance of the lithium recovery process when different types of LiSM are employed. For this analysis, the commercial Selemion CSO membrane was chosen first. This polymeric Cation-Exchange Membrane (CEM) exhibits selectivity towards monovalent cations, thanks to a thin positively charged coating that hinders the transport of multivalent cations, reducing their partitioning coefficient via Donnan exclusion [10,49]. The main properties of the membrane are reported in Table 2. Moreover, to provide further insight into the dependence of the process performance on the LiSM properties, simulations were also performed with an ideal LiSM, sharing the same ionic conductivity of the polymeric Selemion CSO membrane but with a lithium selectivity comparable to the Ohara AG-01 membrane. Indeed, as previously discussed, the main drawback of the Ohara AG-01 membrane is its low ionic conductivity, which significantly limits the SP. The transport properties of both the Selemion CSO and the ideal LiSM were derived from literature data on lithium-selective recovery from multi-ionic solutions using an ED set-up [36], following the procedure described in the Supporting Material. The inferred transport numbers

Table 7
Carbon slurry properties (taken from literature). The volumetric fraction of activated carbon in the slurry (ε_{el}) was evaluated from the available data according to the formula reported in Supporting Material.

Activated Carbon	C_{el} [F/g]	S_{BET} [m^2/g]	ρ_{bulk} [g/mL]	κ_{el} [mS/cm]	ε_{el} [-]
YP-50F	28.6 [45]	1692 [45]	0.30 [45]	0.004 [34]	27 %
YEC-200D	183.7 [42]	2054 [42]	0.40 [46]	0.016 [13]	22 %
Norit SX Ultra	65.0 [47]	1082 [47]	0.32 [48]	0.024 [13]	26 %

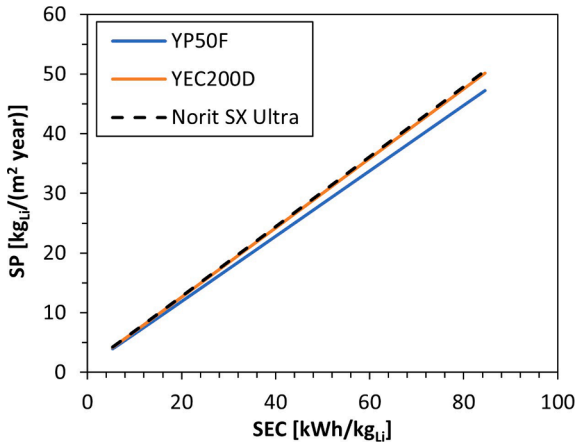

Fig. 8. SP versus SEC for different flow electrode compositions. The simulations were performed changing the applied voltage in the range 0.5–8 V.

are reported in Table 5. To quantify the impact of LiSM transport properties on the lithium recovery process, a process selectivity was defined as follows:

$$S_{Li,i} = \frac{C_{Li,r,out}(t_{tot})/C_{Li,f,out}(0)}{C_{i,r,out}(t_{tot})/C_{i,f,out}(0)} \quad (32)$$

In equation (32), $C_{Li,f,out}(0)$ and $C_{i,f,out}(0)$ are respectively the concentration of lithium and the generic species i in the feed tank at the beginning of the test, while $C_{i,r,out}(t_{tot})$ and $C_{i,r,out}(t_{tot})$ are evaluated at the end of the test. The process selectivity achieved with the three different LiSM is reported in Fig. 9.

Clearly, the performance of the Selemion CSO is the worst among the membrane simulated. Particularly, Li/Na and Li/K selectivity approach

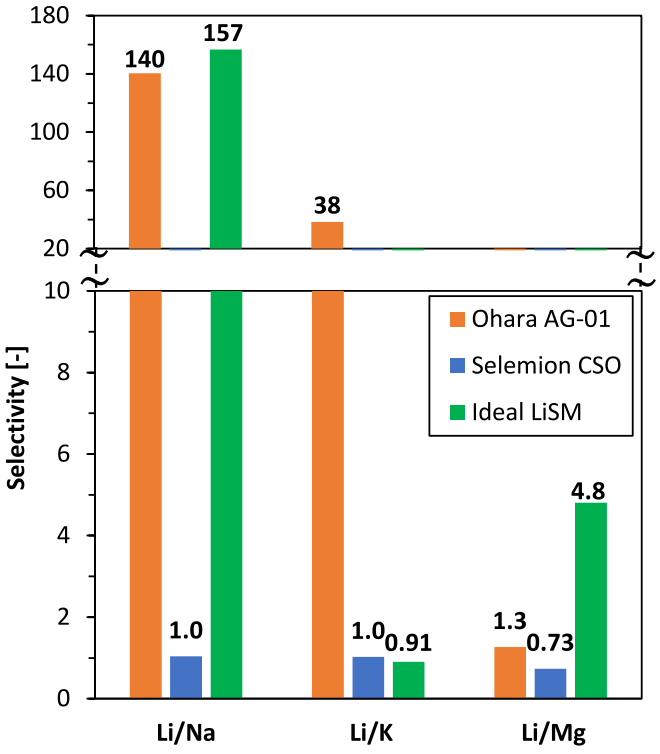

Fig. 9. Process selectivity achieved using different LiSMs. All the simulations were performed at similar process conditions in terms of test duration (7 days), applied voltage (1.2 V) and flow rates (10 mL/min for feed and receiver, 100 mL/min for flow electrodes).

unity, implying that the membrane exhibits no selectivity towards specific monovalent species. The poor lithium selectivity may be attributed to the composition of the membrane: the CSO membrane is a charged polymeric membrane, whose ion selectivity is primarily governed by electrostatic and dielectric effects [49,50]. Li^+ has a higher charge density than Na^+ and K^+, which leads to a lower affinity of lithium ions for the membrane. The results clearly indicate that conventional polymeric membranes cannot be used to effectively separate lithium from other competing monovalent cations. On the other hand, the Ohara AG-01 membrane exhibits excellent Li/Na and Li/K selectivity due to its selectivity mechanism, primarily based on a steric size-dependent effect, that hinders the transport of the ions with an effective radius higher than that of Li^+. However, one of the drawbacks of this ceramic membrane is its inability to block Mg^{2+} ions, given that Mg^{2+} and Li^+ have comparable ionic radii. This results in poor Li/Mg selectivity. Indeed, the difference in selectivity must be attributed to the different nature of the membranes. From an industrial standpoint, the use of a ceramic LiSM, such as the one simulated, would require a prior treatment step to separate the Mg^{2+} ions, for instance, through reactive crystallization technologies [51]. When considering the performance of the ideal LiSM, the Li/Na and Li/K selectivity are comparable to those of the Ohara AG-01, yet its Li/Mg is significantly high. This result stems from the fact that the chosen ideal LiSM has transport properties comparable to a Selemion CSO membrane equilibrated with an equimolar mixture of Na^+, K^+, Li^+ and Mg^{2+}, as reported in the Supporting Material. Since CSO is a monovalent selective membrane, the ideal LiSM is effectively able to hinder the Mg^{2+} ion passage through electrostatic repulsion mechanism. Such kind of ideal LiSM could be obtained for instance by doping polymeric monovalent-selective IEMs with solid-state electrolytes [52] to achieve lithium selectivity comparable to a ceramic membrane. Further comparisons of the performances of the three different membranes, in terms of SEC and SP, were carried out by simulating different applied voltages and feed and receiver flow rates. The results are presented in Fig. 10.

As it can be seen in Fig. 10A, the SEC achieved with the CSO membrane is almost 2 orders of magnitudes higher than the one achieved with the ceramic membrane, primarily because of the different current densities achieved The ionic conductivity of the CSO membrane, in fact, is several orders of magnitude higher than that of the AG-01 membrane. However, given the low Li/Na selectivity of the membrane, most of the electrical current is associated with the transport of Na^+ to the receiver compartment, resulting in a very poor SEC. Specifically, the higher current density, mainly driven by Na^+ ions transport, drastically increases the electrical power required per unit mass of lithium recovered. Moreover, the Selemion CSO SEC is insensitive toward the flow rates, meaning that polarization phenomena have negligible effect on SEC. This can be easily explained considering that Na^+, which carries most of the electrical current, is the most abundant species in the system. Therefore, polarization phenomena at the LiSM interface are limited. Similarly, SP and SEC of the Ohara AG-01 are not influenced by the flowrates because, as explained in the previous sections, the high membrane resistance reduces the current density and consequently mitigates the effect of the polarization phenomena. In contrast, the SEC obtained with the ideal LiSM, which has an ionic resistance comparable to that of a conventional polymeric membrane, is significantly reduced when increasing the flowrates from 10 to 100 mL/min, especially at high applied voltage. Particularly, the effect of the polarization phenomena accounts for about 63 % of the SEC at 4 V and at a feed flow rate of 10 mL/min. The same value drops to 30 % if the flow rate is increased to 100 mL/min. This major outcome difference between the two membranes must be attributed to the different magnitudes of polarization phenomena occurring at the membranes' interfaces, due to the difference in the ionic conductivity of the two membranes. As the current density achieved with the ideal LiSM membrane is about one order of magnitude higher (1.2 A/m^2 A vs 0.1 A/m^2 at 1.2 V) than the one obtained with the AG-01 membrane, the polarization phenomena are more pronounced and hence, the effect of flow rates on the SEC is more evident. This analysis is also consistent with the SP vs voltage trend shown in Fig. 10B. The SP achieved with the AG-01 membrane is lower and insensitive toward the flow rates due to the low current densities achieved. On the contrary, the SP of the ideal LiSM is higher and strongly dependent on the applied flow rates. Moreover, at high external voltage, the SP achieves a plateau value dependent on the flow rates of the solutions. This is clearly due to the achievement of the limiting current regime for lithium at which, an increase in the applied voltage does not produce any increase in the lithium flux across the LiSM. Consequently, the SP remains constant even though the SEC keeps increasing due to the net increase in the overall current, which is supported by the ionic fluxes of the other species. The plateau in lithium productivity can be enhanced by increasing the flow rate. In particular, by increasing the flowrates

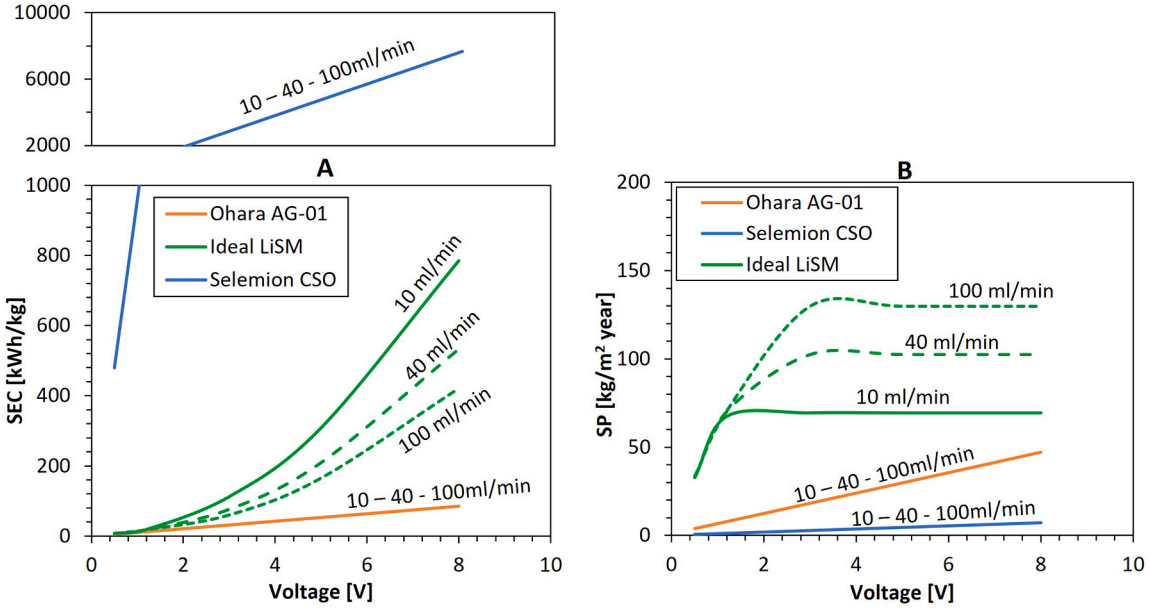

Fig. 10. (A) Ohara AG-01, Selemion CSO and Ideal LiSM SEC versus external voltage at different feed and receiver flow rates. (B) Ohara AG-01, Selemion CSO and Ideal LiSM SP versus external voltage at different flow rates. Feed and receiver flow rates are set equal and changed simultaneously.

from 10 to 100 mL/min, the limiting SP is increased by 89 %. Indeed, the lithium limiting current density is equal to 1.31 A/m^2 at 10 mL/min, while it increases to 2.82 A/m^2 at 100 mL/min of feed flow rate. Therefore, at high applied voltage and low flow rates, a reduction in lithium selectivity is expected. To corroborate this thesis, the lithium selectivity of the ideal LiSM membrane against the applied voltage and flow rates was reported in Fig. 11.

From Fig. 11 it is evident that the lithium selectivity decreases at high applied voltage, i.e., at high current density, demonstrating that working at higher applied voltage would be inconvenient. This happens because the limited amount of lithium in the feed solution reduces the maximum lithium partial limiting current density. Indeed, according to the definition of polarization coefficient (equation (12)), the polarization phenomena are more pronounced for the species with either the highest transport number (i.e., with the highest membrane selectivity) [53] in the membrane or the lowest concentration in the bulk solution. Consequently, at fixed external voltage, an increase in the flow rates leads to an increment in Li/Na and Li/K selectivity because, in terms of transport rate, the reduction of the DBL thickness is more beneficial for Li^+ than for Na^+ or K^+. Regarding the Li/Mg selectivity, the higher values achieved at 1.2 V compared to the selectivity achieved at 0.5 V can be explained considering that, at fixed transport numbers, the moles of Li^+ recovered per unit of charge is double that of Mg^{2+}. Hence, an increase in the applied voltage, i.e., an increase in the current density, causes an increase in the process selectivity. The same does not occur at 5 mL/min of flow rates because the polarization phenomena reduce the lithium flux and hence the process selectivity. Interestingly, at high external voltage there is a slight decrease of Li/Mg selectivity at increasing flow rates. The effect of polarization phenomena on the actual membrane selectivity has already been investigated by several authors [28,49] who have reported an increased selectivity of cations with lower mobility in water at increasing flow rates. This nontrivial point may be explained considering the order of bulk mobility of the cations considered in the present study (K^+>Na^+>Li^+>Mg^{2+}), which is related to their hydrated radii. Mg^{2+} has a lower mobility compared to Li^+ and consequently, an increase in flow rate would be more beneficial for the transport rate of magnesium across the DBL than for lithium. In fact, the polarization coefficient tends to decrease as the diffusivity in the solution increases. Indeed, polarization phenomena must be considered when performing a selective recovery of trace elements, such as lithium. In the case of the ideal LiSM membrane, for example, an increase in voltage from 1.2 to 3 V can lead to an increase in SP. However, this increase may result in a significant reduction in selectivity, which could be unacceptable. When reaching the limiting regime, the process selectivity tends toward a value that, rather than being dependent on the membrane selectivity, is significantly influenced by the applied current density and the flow regime [49].

5. Conclusions

In this work, a simple, flexible, and easy to implement pseudo steady-state model for selective lithium recovery with a FCDI unit was developed. The model was successfully calibrated against experimental data collected in SC closed-loop configuration. The results showed that the performance of the Li-MFCDI unit equipped with the Ohara AG-01 membrane was mainly influenced by the extremely high resistivity of the solid-state LiSM. Despite high Li/Na and Li/K selectivities achieved, low lithium flux is an limitation when using Ohara AG-01 membrane.

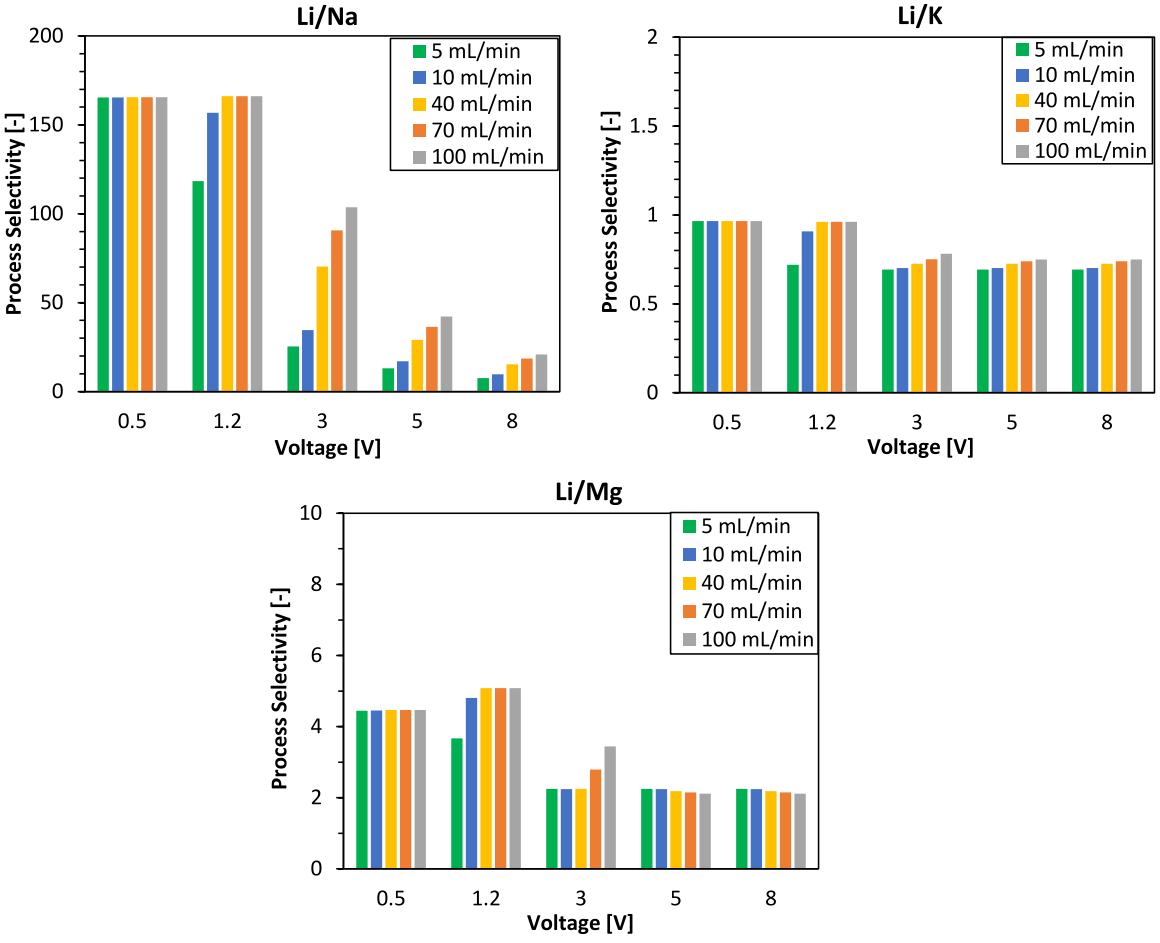

Fig. 11. Li/Na, Li/K and Li/Mg selectivity of the ideal LiSM versus applied voltage and feed and receiver flow rates.

The simulations demonstrated that acceptable lithium selectivity cannot be achieved when using currently available commercial, mono-selective polymeric CEM.

However, using an ideal monovalent-selective polymeric membrane, the lithium selectivity would be comparable to the Ohara AG-01 membrane. The simulations showed that lithium productivity rises by more than 1 order of magnitude if the membrane ionic conductivity is increased up to the average values of a standard polymeric membrane. Furthermore, with low-resistive membranes, both SP and selectivity are significantly affected by the flow rate and applied voltage (with the effect of the applied voltage being predominant). Ultimately, the proposed theoretical model is a robust tool for process simulations aimed at optimizing lithium recovery from multi-ionic brines. The proposed model does not account for the occurrence of Faradaic processes at the electrodes, concentration polarization within the electrode compartments, and hydraulic calculations. In future, such phenomena should be incorporated to enhance the model's predictive capabilities.

CRediT authorship contribution statement

Giorgio Purpura: Conceptualization, Data curation, Formal analysis, Investigation, Methodology, Software, Validation, Writing – original draft. **Hafiz Muhamad Saif:** Data curation, Formal analysis, Investigation, Methodology, Writing – original draft. **Andrea Culcasi:** Conceptualization, Methodology, Software, Supervision, Validation, Writing – review & editing. **Sylwin Pawlowski:** Conceptualization, Formal analysis, Methodology, Supervision, Writing – review & editing. **Joao Goulão Crespo:** Conceptualization, Funding acquisition, Resources, Supervision, Writing – review & editing. **Andrea Cipollina:** Conceptualization, Methodology, Project administration, Resources, Supervision, Writing – review & editing.

Declaration of competing interest

The authors declare that they have no known competing financial interests or personal relationships that could have appeared to influence the work reported in this paper.

Acknowledgements

This work received funding from the European Union Horizon 2020 research and innovation programme under grant agreement No 869467 (SEArcularMINE).

This work was also supported by the Associate Laboratory for Green Chemistry – LAQV (UIDB/50006/2020) and grant agreement No PTDC/EQU-EQU/6193/2020 (Se(L)ect(i)vity), both financed by national Portuguese funds from FCT/MCTES. Hafiz Muhammad Saif Ullah Saleem additionally acknowledges FCT/MCTES for his PhD grant 2020.09828.BD (Doi: 10.54499/2020.09828.BD).

Appendix A. Supplementary data

Supplementary data to this article can be found online at https://doi.org/10.1016/j.seppur.2025.132400.

Data availability

Data will be made available on request.

References

[1] J. Si, C. Xue, S. Li, L. Yang, W. Li, J. Yang, J. Lan, N. Sun, Selective membrane capacitive deionization for superior lithium recovery, Desalination 572 (2023) 117154, https://doi.org/10.1016/j.desal.2023.117154.

[2] X. Guo, J. Zhang, Q. Tian, Modeling the potential impact of future lithium recycling on lithium demand in China: a dynamic SFA approach, Renew. Sustain. Energy Rev. 137 (2021) 110461, https://doi.org/10.1016/j.rser.2020.110461.

[3] M.L. Vera, W.R. Torres, C.I. Galli, A. Chagnes, V. Flexer, Environmental impact of direct lithium extraction from brines, Nat. Rev. Earth Environ. 4 (2023) 149–165, https://doi.org/10.1038/s43017-022-00387-5.

[4] A. Cipollina, D. Winter, G. Battaglia, L. Berkemeyer, J.L. Cortina, M.F. de Labastida, J.L. Rodriguez, Recovery of lithium carbonate from Dilute Li-Rich Brine via homogenous and heterogeneous precipitation, Ind. Eng. Chem. Res. 61 (2022) 13589–13602, https://doi.org/10.1021/acs.iecr.2c01397.

[5] S. Randazzo, F. Vicari, J. López, M. Salem, R. Lo Brutto, S. Azzouz, S. Chamam, S. Cataldo, N. Muratore, M. Fernández de Labastida, V. Vallès, A. Pettignano, G. D'Alì Staiti, S. Pawlowski, A. Hannachi, J.L. Cortina, A. Cipollina, Unlocking hidden mineral resources: characterization and potential of bitterns as alternative sources of critical raw materials, J. Clean. Prod. 436 (2024), https://doi.org/10.1016/j.jclepro.2023.140412.

[6] Y. Guo, Y. Ying, Y. Mao, X. Peng, B. Chen, Polystyrene sulfonate threaded through a metal–organic framework membrane for fast and selective lithium-ion separation, Angew. Chemie - Int. Ed. 55 (2016) 15120–15124, https://doi.org/10.1002/anie.201607329.

[7] H. Strathmann, Ion-Exchange membrane separation processes, First, Elsevier B.V. 2004.

[8] A. Campione, L. Gurreri, M. Ciofalo, G. Micale, A. Tamburini, A. Cipollina, Electrodialysis for water desalination: a critical assessment of recent developments on process fundamentals, models and applications, Desalination 434 (2018) 121–160, https://doi.org/10.1016/j.desal.2017.12.044.

[9] S. Ozkul, J.J. van Daal, N.J.M. Kuipers, R.J.M. Bisselink, H. Bruning, J.E. Dykstra, H.H.M. Rijnaarts, Transport mechanisms in electrodialysis: the effect on selective ion transport in multi-ionic solutions, J. Memb. Sci. 665 (2023) 121114, https://doi.org/10.1016/j.memsci.2022.121114.

[10] J.G. Gamaethiralalage, K. Singh, S. Sahin, J. Yoon, M. Elimelech, M.E. Suss, P. Liang, P.M. Biesheuvel, R.L. Zornitta, L.C.P.M. De Smet, Recent advances in ion selectivity with capacitive deionization, Energy Environ. Sci. 14 (2021) 1095–1120, https://doi.org/10.1039/d0ee03145c.

[11] S. Il Jeon, H.R. Park, J.G. Yeo, S. Yang, C.H. Cho, M.H. Han, D.K. Kim, Desalination via a new membrane capacitive deionization process utilizing flow-electrodes, Energy Environ. Sci. 6 (2013) 1471–1475, https://doi.org/10.1039/c3ee24443a.

[12] J. Ma, C. Zhang, F. Yang, X. Zhang, M.E. Suss, X. Huang, P. Liang, Carbon black flow electrode enhanced electrochemical desalination using single-cycle operation, Environ. Sci. Technol. 54 (2020) 1177–1185, https://doi.org/10.1021/acs.est.9b04823.

[13] F. Yang, Y. He, L. Rosentsvit, M.E. Suss, X. Zhang, T. Gao, P. Liang, Flow-electrode capacitive deionization: a review and new perspectives, Water Res. 200 (2021) 117222, https://doi.org/10.1016/j.watres.2021.117222.

[14] C. Zhang, J. Ma, L. Wu, J. Sun, L. Wang, T. Li, T.D. Waite, Flow Electrode Capacitive Deionization (FCDI): recent developments, environmental applications, and future perspectives, Environ. Sci. Technol. 55 (2021) 4243–4267, https://doi.org/10.1021/acs.est.0c06552.

[15] H.M. Saif, T.H. Gebregeorgis, J.G. Crespo, S. Pawlowski, The influence of flow electrode channel design on flow capacitive deionization performance: experimental and CFD modelling insights, Desalination 578 (2024) 117452, https://doi.org/10.1016/j.desal.2024.117452.

[16] H.M. Saif, J.G. Crespo, S. Pawlowski, Lithium recovery from brines by lithium membrane flow capacitive deionization (Li-MFCDI) – a proof of concept, J. Membr. Sci. Lett. 3 (2023) 100059, https://doi.org/10.1016/j.memlet.2023.100059.

[17] A. Rommerskirchen, B. Ohs, K.A. Hepp, R. Femmer, M. Wessling, Modeling continuous flow-electrode capacitive deionization processes with ion-exchange membranes, J. Memb. Sci. 546 (2018) 188–196, https://doi.org/10.1016/j.memsci.2017.10.026.

[18] L. Wang, C. Zhang, C. He, T.D. Waite, S. Lin, Equivalent film-electrode model for flow-electrode capacitive deionization: experimental validation and performance analysis, Water Res. 181 (2020) 115917, https://doi.org/10.1016/j.watres.2020.115917.

[19] A. Filingeri, J. Lopez, A. Culcasi, T. Leon, A. Tamburini, J. Luis Cortina, G. Micale, A. Cipollina, In-depth insights on multi-ionic transport in Electrodialysis with bipolar membrane systems, Chem. Eng. J. 468 (2023), https://doi.org/10.1016/j.cej.2023.143673.

[20] A. Culcasi, L. Gurreri, A. Zaffora, A. Cosenza, A. Tamburini, G. Micale, On the modelling of an acid/base flow battery: an innovative electrical energy storage device based on ph and salinity gradients, Appl. Energy. 277 (2020) 115576, https://doi.org/10.1016/j.apenergy.2020.115576.

[21] Fumatech, f u m a s e p ® F A B - P K - 1 3 0, (2018) 24–25. http://www.fuelcellstore.com/spec-sheets/fumasep-fab-pk-130-technical-specifications.pdf.

[22] K. Kontturi, L. Murtomäki, J.A. Manzanares, Ionic transport processes: in electrochemistry and membrane science, Ion. Transp. Process. Electrochem. Membr. Sci. 9780199533 (2008) 1–304, https://doi.org/10.1093/acprof:oso/9780199533817.001.0001.

[23] M.J. Rice, W.L. Roth, Ionic transport in super ionic conductors: a theoretical model, J. Solid State Chem. 4 (1972) 294–310, https://doi.org/10.1016/0022-4596(72)90121-1.

[24] O.L. Anderson, D.A. Stuart, Calculation of activation energy of ionic conductivity in silica glasses by classical methods, J. Am. Ceram. Soc. 37 (1954) 573–580, https://doi.org/10.1111/j.1151-2916.1954.tb13991.x.

[25] Y. Tanaka, Ion Exchange Membranes: Fundamentals and Applications: Second Edition. 2015. Doi: 10.1016/C2013-0-12870-X.

[26] R.S. Kingsbury, O. Coronell, Modeling and validation of concentration dependence of ion exchange membrane permselectivity: significance of convection and Manning's counter-ion condensation theory, J. Memb. Sci. 620 (2021) 118411, https://doi.org/10.1016/j.memsci.2020.118411.

[27] M.L. La Cerva, M. Di Liberto, L. Gurreri, A. Tamburini, A. Cipollina, G. Micale, M. Ciofalo, Coupling CFD with a one-dimensional model to predict the performance of reverse electrodialysis stacks, J. Memb. Sci. 541 (2017) 595–610, https://doi.org/10.1016/j.memsci.2017.07.030.
[28] D. Ding, L. Yang, J. Wang, A. Yaroshchuk, J.L. Schaefer, M.L. Bruening, Selective transport of trivalent lanthanide in electrodialysis: limitations due to concentration polarization, J. Memb. Sci. 685 (2023) 121949, https://doi.org/10.1016/j.memsci.2023.121949.
[29] S. Pawlowski, P. Sistat, J.G. Crespo, S. Velizarov, Mass transfer in reverse electrodialysis: flow entrance effects and diffusion boundary layer thickness, J. Memb. Sci. 471 (2014) 72–83, https://doi.org/10.1016/j.memsci.2014.07.075.
[30] E. Volodina, N. Pismenskaya, V. Nikonenko, C. Larchet, G. Pourcelly, Ion transfer across ion-exchange membranes with homogeneous and heterogeneous surfaces, J. Colloid Interface Sci. 285 (2005) 247–258, https://doi.org/10.1016/j.jcis.2004.11.017.
[31] R. De Levie, The influence of surface roughness of solid electrodes on electrochemical measurements, Electrochim. Acta. 10 (1965) 113–130, https://doi.org/10.1016/0013-4686(65)87012-8.
[32] S. Fletcher, V.J. Black, I. Kirkpatrick, A universal equivalent circuit for carbon-based supercapacitors, J. Solid State Electrochem. 18 (2014) 1377–1387, https://doi.org/10.1007/s10008-013-2328-4.
[33] A.K.E. Rommerskirchen, Continuous Flow-Electrode capacitive deionization, Aachener Verfahrenstechnik Ser. AVT.CVT – Chem. Process Eng. 12 (2021), https://doi.org/10.18154/RWTH-2021-02093.
[34] S. Porada, D. Weingarth, H.V.M. Hamelers, M. Bryjak, V. Presser, P.M. Biesheuvel, Carbon flow electrodes for continuous operation of capacitive deionization and capacitive mixing energy generation, J. Mater. Chem. A. 2 (2014) 9313–9321, https://doi.org/10.1039/c4ta01783h.
[35] R.B. McCleskey, D.K. Nordstrom, J.N. Ryan, J.W. Ball, A new method of calculating electrical conductivity with applications to natural waters, Geochim. Cosmochim. Acta. 77 (2012) 369–382, https://doi.org/10.1016/j.gca.2011.10.031.
[36] X.Y. Nie, S.Y. Sun, Z. Sun, X. Song, J.G. Yu, Ion-fractionation of lithium ions from magnesium ions by electrodialysis using monovalent selective ion-exchange membranes, Desalination 403 (2017) 128–135, https://doi.org/10.1016/j.desal.2016.05.010.
[37] A. Filingeri, M. Philibert, E. Filloux, N. Moe, A. Poli, A. Tamburini, A. Cipollina, Valorization of surface-water RO brines via Assisted-Reverse Electrodialysis for minerals recovery: performance analysis and scale-up perspectives, Desalination 541 (2022) 116036, https://doi.org/10.1016/j.desal.2022.116036.
[38] C. Shi, H. Wang, A. Li, G. Zhu, X. Zhao, F. Wu, Process model for flow-electrode capacitive deionization for energy consumption estimation and system optimization, Water Res. 230 (2023), https://doi.org/10.1016/j.watres.2022.119517.
[39] D.Y. Butylskii, V.A. Troitskiy, N.V. Smirnova, N.D. Pismenskaya, Y. Wang, C. Jiang, T. Xu, V.V. Nikonenko, Review of recent progress on lithium recovery and recycling from primary and secondary sources with membrane-based technologies, Desalination 586 (2024), https://doi.org/10.1016/j.desal.2024.117826.
[40] H.J. Cassady, E.C. Cimino, M. Kumar, M.A. Hickner, Specific ion effects on the permselectivity of sulfonated poly(ether sulfone) cation exchange membranes, J. Memb. Sci. 508 (2016) 146–152, https://doi.org/10.1016/j.memsci.2016.02.048.
[41] M. Galizia, F.M. Benedetti, D.R. Paul, B.D. Freeman, Monovalent and divalent ion sorption in a cation exchange membrane based on cross-linked poly (p-styrene sulfonate-co-divinylbenzene), J. Memb. Sci. 535 (2017) 132–142, https://doi.org/10.1016/j.memsci.2017.04.007.
[42] K. Zhang, J. Sun, L. E, C. Ma, S. Luo, Z. Wu, W. Li, S. Liu, Effects of the pore structure of commercial activated carbon on the electrochemical performance of supercapacitors, J. Energy Storage. 45 (2022) 103457, https://doi.org/10.1016/j.est.2021.103457.
[43] N. Ganfoud, A. Sene, M. Haefele, A. Marin-Laflèche, B. Daffos, P.L. Taberna, M. Salanne, P. Simon, B. Rotenberg, Effect of the carbon microporous structure on the capacitance of aqueous supercapacitors, Energy Storage Mater. 21 (2019) 190–195, https://doi.org/10.1016/j.ensm.2019.05.047.
[44] H. Wu, M. Genovese, K. Ton, K. Lian, A comparative study of activated carbons from liquid to solid polymer electrolytes for electrochemical capacitors, J. Electrochem. Soc. 166 (2019) A821–A828, https://doi.org/10.1149/2.0141906jes.
[45] Kuraray Coal Tm, (2019) 2019. https://www.calgoncarbon.com/app/uploads/YP-brochure-draft_final_08_2019.pdf.
[46] Fuzhou Yihuan Carbon, (2024). http://www.yhcarbon.com/index.php?m=home&c=View&a=index&aid=89 (accessed April 19, 2024).
[47] B. Fang, Hierarchical nanostructured carbon materials for ultrahigh electrical charge storage, ECS Meet. Abstr. MA2013-02 (2013) 655, https://doi.org/10.1149/MA2013-02/9/655.
[48] Lerochem - Chemical supply, No Title, (2019). https://lerochem.eu/en/pagrindinis/336-1136-activated-carbon-farm-grade-kg.html (accessed April 28, 2024).
[49] T. Luo, S. Abdu, M. Wessling, Selectivity of ion exchange membranes: a review, J. Memb. Sci. 555 (2018) 429–454, https://doi.org/10.1016/j.memsci.2018.03.051.
[50] H. Zhang, G.M. Geise, Modeling the water permeability and water/salt selectivity tradeoff in polymer membranes, J. Memb. Sci. 520 (2016) 790–800, https://doi.org/10.1016/j.memsci.2016.08.035.
[51] G. Battaglia, L. Ventimiglia, F.P.M. Viggiano, F. Vassallo, A. Cipollina, A. Tamburini, G. Micale, Mg(OH)2 recovery from real bitterns: a proof of concept at pilot scale, Chem. Eng. Trans. 105 (2023) 1–6, https://doi.org/10.3303/CET23105001.
[52] H.M. Saif, R.M. Huertas, S. Pawlowski, J.G. Crespo, S. Velizarov, Development of highly selective composite polymeric membranes for Li+/Mg2+ separation, J. Memb. Sci. 620 (2021) 118891, https://doi.org/10.1016/j.memsci.2020.118891.
[53] T. Luo, F. Roghmans, M. Wessling, Ion mobility and partition determine the counter-ion selectivity of ion exchange membranes, J. Memb. Sci. 597 (2020) 117645, https://doi.org/10.1016/j.memsci.2019.117645.